Flat electron mirror

Krielaart, M. A.R.; Kruit, P.

DOI
10.1016/j.ultramic.2020.113157

Publication date
2021

Document Version
Final published version

Published in
Ultramicroscopy

Ultramicroscopy 220 (2021) 113157

Contents lists available at ScienceDirect

Ultramicroscopy

journal homepage: www.elsevier.com/locate/ultramic

Flat electron mirror

M.A.R. Krielaart *, P. Kruit

Department of Imaging Physics, Delft University of Technology, Lorentzweg 1, 2628CJ Delft, The Netherlands

ARTICLE INFO

Keywords:
Tetrode electron mirror
Spot size calculations
Patterned electron mirrors

ABSTRACT

Electron beams can be reflected by an electrode that is at a more negative potential than the cathode from which the beam is emitted. We want to design a mirror with a flat mirror electrode where the electrons are reflected at a plane very close to the electrode. The wave front of an electron can then be shaped when the mirror contains a surface topography or modulated potential. However, electron beams reflected by flat electron mirrors are usually characterized by high coefficients of chromatic and spherical aberration. When the mirror is combined with an electrostatic lens to form a tetrode mirror system, the situation deteriorates even further. This places a restrictive limit on the maximum aperture angle of the beam, and consequently also limits the attainable resolution at the image plane. We have numerically studied the dependence of these aberrations as a function of design parameters of the tetrode mirror consisting of a ground, lens, cap, and mirror electrode, and limited ourselves to only using flat electrodes with round apertures, at fixed electrode spacing. It turns out that the third order spherical aberration can be made negative. The negative third order aberration is then used to partially compensate the positive fifth order aberration. This way, a system configuration is obtained that, at 2 keV beam energy, provides a diffraction limited resolution of 7.6 nm at an image plane 25 mm from the mirror at beam semi-angles of 2.3 mrad, enabling an illumination radius of 40 μm at the mirror. The presented tetrode mirror design could spark innovative use of patterned electron mirrors as phase plates for electron microscopy in general, and for use as coherent beam splitters in Quantum Electron Microscopy in particular. An appendix presents a method to calculate the spot size of a focused beam in the presence of both third and fifth order spherical aberration coefficients, which is also applicable to Scanning (Transmission) Electron Microscopes with aberration correctors.

1. Introduction

An electron beam is reflected at an equipotential surface, under the condition that the electric potential matches that of the electron beam acceleration voltage. Mirror electron microscopy (MEM) [1,2] schemes revolve around this principle, and derived techniques are mainly applied in the field of surface physics [3–5]. In one mode of operation, the specimen is kept at a bias potential that is slightly more negative than the beam acceleration voltage, so that the equipotential surface of reflection closely resembles the surface topography or structure of the specimen. It is the modulation of the reflection field that imprints a spatial phase distribution in the reflected beam. By imaging the reflected beam onto a detector the imprinted phase distribution offers information about the specimen.

The former principle can also be reversed. By carefully sculpting a topographic pattern into a mirror substrate, the modulation of the electric field can be controlled. Current research focuses on using topographically patterned grating mirrors [6] that can act as beam splitters and recombiners in quantum electron microscopy (QEM) [7]. QEM constitutes an interaction-free measurement scheme that is based on multiple passes through a Mach–Zehnder type interferometer [8]. The grating mirror is then part of an electron resonator [Fig. 1] in which repetitive reflection of the beam at the mirror allows for the gradual transition of amplitude between the sample and reference beam of the interferometer [9].

Electron mirrors are more typically used for the correction of axial chromatic and spherical aberrations [11]. This can be achieved with a concave shaped electric field, which can be created for instance by using an aperture with a radius much larger than the beam envelop as a mirror electrode. Another approach, for which an analytical solution to the shape of the electric field can be provided, is realized by making a cone-shaped indentation in the mirror electrode [12]. The latter is however more mechanically challenging, when compared to machining a round aperture.

Unfortunately, (nearly) flat mirror surfaces as found in the linear QEM resonator are usually characterized by large coefficients of spherical and chromatic aberration. When the mirror is positioned in the

* Corresponding author.
E-mail address: m.a.r.krielaart@tudelft.nl (M.A.R. Krielaart).

https://doi.org/10.1016/j.ultramic.2020.113157
Received 4 August 2020; Received in revised form 21 October 2020; Accepted 27 October 2020
Available online 2 November 2020

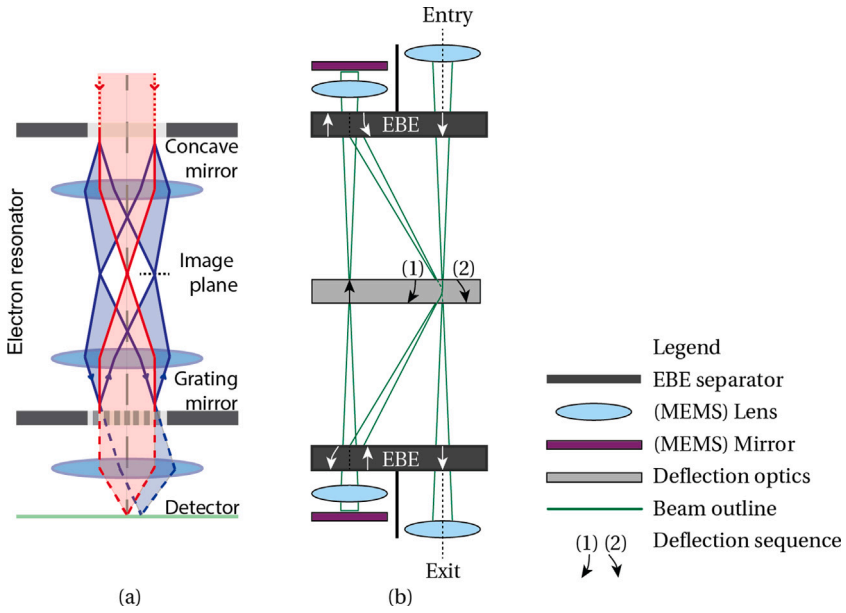

Fig. 1. Principle and schematic design of a linear QEM resonator. (a) The electron beam enters the cavity through a temporally gated electron mirror. The central beam is diffracted at the lower mirror element, and the diffracted beam is repeatedly imaged onto the image plane. Based on the system in [7]. (b) Practical design of a linear QEM cavity that requires no temporal gating of the mirror potential. Instead, a low-voltage electrostatic deflector to the right side of the image plane enables the in-coupling, cycling, and out-coupling of the beam. Based on a system in [10].

diffraction plane of an imaging system, as is the case for grating mirrors for QEM, the high aberration coefficients will result in loss of resolution at the image plane. In an electron resonator system, a second electron mirror that provides a concave reflection field can correct for these aberrations [12–15] when positioned in the conjugate plane of the flat mirror. A schematic design of such system [7,16] is shown in [Fig. 1].

In principle, the required field shape of the aberration correcting mirror can be provided by the patterned (first) mirror as well. This would eliminate the need for the second mirror or the second mirror could be used for a different purpose. For this, one has to obtain the shape of the concave equipotential surface of the aberration correcting mirror at the potential of the patterned mirror. The shape of this equipotential surface can then be added to any topography that is already present on the first mirror. Alternatively, when using a mirror with a modulated potential, the aberration correction can be added as a radial potential distribution. However, especially when the desired pattern on the electron's phase front contains small features, such as the line pattern for the grating, it seems better to start with an atomically flat surface at a single potential.

The difficulty of combining spatial frequencies that range over multiple decades stems from the drop in field modulation in the longitudinal direction, perpendicular to the mirror substrate [6]. In the above example, the grating pattern for creating diffraction would require a line profile amplitude in the order of 100 nm, while the profile amplitude for the aberration correction would be in the order of single-digit nanometers, making it very difficult to fabricate.

Thus, it would be much preferable to have a mirror design with a flat mirror electrode that has no axial aberrations. Earlier, van Aken et al. suggested that aberrations can be corrected for when a slow electron beam is transmitted elastically through a flat thin foil [17,18], at energies well below 1 eV. This requires that the foil is maintained at a potential that is close to the acceleration voltage of the beam. The corrective properties are then obtained by a careful choice of the foil and lens geometry. The geometry of such low-voltage foil corrector must satisfy the critical condition $s \ll R_C$, with s the longitudinal spacing between the foil and the field limiting cap aperture, and R_C the radius of this aperture.

The low-voltage foil corrector provides for axial aberration correction and the basic geometry shows close resemblance to a tetrode electron mirror [Fig. 2(a)] that is found in a QEM resonator. For this reason we believe that it is possible to correct for the combined axial aberrations of tetrode mirror systems by means of the mechanical configuration.

In the past, exotic shapes for the lens element apertures were considered in order to tune the axial aberrations of the tetrode mirror [19,20]. Here, we consider only plane through-hole apertures [Fig. 2(b)], and at fixed electrode spacing for the lens elements. Modern day lithographic processes have found their way into the manufacturing of very round miniature apertures [21], which allows for an easy means of tuning the aperture radius in a production process. Meanwhile, the axial separation of the distinct miniature apertures is limited by the available dimensions of flat spacer elements. For this reason, we only study the axial aberration properties of tetrode mirror systems for a range of aperture radii and potentials, at fixed aperture spacing.

We performed a numerical study with the model system that is shown in [Fig. 2(b)]. It consists of the flat mirror electrode and three thin plates with apertures. We have a lot of experience with making electron lens electrodes from silicon wafers using lithography and etch processes. We are able to etch apertures of typically 0.1 to 1 mm diameter with a roundness better than 1 μm which we can also align to within 1 μm.

2. Basic concepts

For the electron resonator design, and for repetitive imaging in QEM, we require that the image plane coincides with the front focal plane of the focusing lens of the mirror system. This enables symmetric ray trajectories that provide the re-imaging of the reflected beam back onto the sample plane, with 1x magnification [Fig. 2(a)]. As we assume that the specimen is positioned in a field free region, we need at least three lens electrodes for the lens design.

The first electrode (that is positioned closest to the sample plane) provides the boundary to the field free region on the left. Without at least this one electrode, a symmetric ray trajectory can never be obtained. The second element performs the lens action. In principle, the third lens element may be omitted. However, the inclusion of the third element (positioned closest to the mirror) provides a second degree of freedom in the electric excitation of the lens that will allow

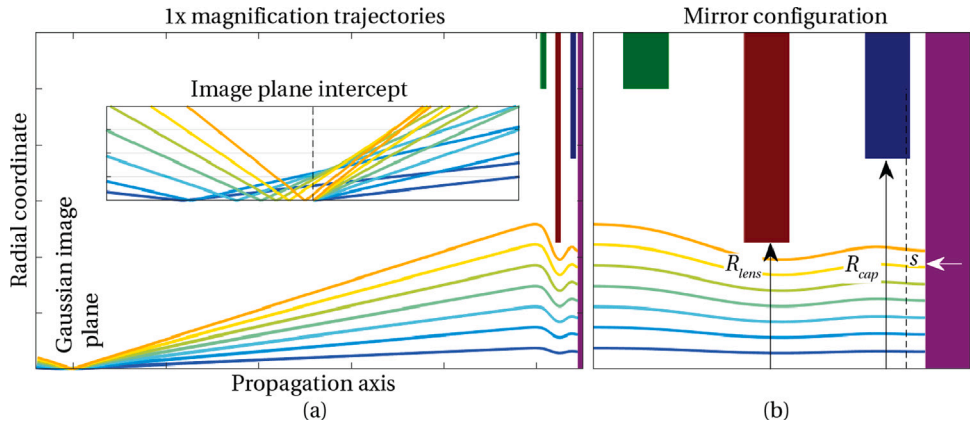

Fig. 2. (a) Ray trajectories at 1x magnification and for coinciding object and image (sample) plane. The front focal plane of the lens coincides with these planes. The inset contains details of the ray trajectories near the Gaussian image plane. (b) Schematic overview of the mechanical configuration of a tetrode electron mirror (rotational symmetric around the propagation axis), with labels for aperture electrode radii R and spacing between the mirror and cap electrode s. Elements are identified as (green) ground, (red) lens, (blue) cap, and (purple) mirror electrode. The radial coordinate of the trajectories is magnified by factor 3. Horizontal and vertical axes are not to equal scale. (For interpretation of the references to color in this figure legend, the reader is referred to the web version of this article.)

to simultaneously alter the strength of the mirror electric field to the right, while also maintaining the 1x magnification re-imaging onto the sample plane. We call this third element the 'cap electrode'.

The ability to tune the linear electric field strength in between the cap and mirror electrode allows for adjusting the longitudinal spacing between equipotential planes in front of the mirror [19]. Consequently, this influences the turning points and ray trajectories for a polychromatic beam and offers a degree of freedom for tuning the chromatic aberrations of the electron mirror. The object and image planes coincide with the front focal plane of the lens, thus placing the mirror electrode in the Fourier plane of the lens. For a 1x magnification, this necessarily results in a collimated beam at the mirror plane, hence we refer to the lens as a collimator.

The spot size at the image plane is determined by the semi-angle of the beam. A spot size contribution due to diffraction is unavoidable, but is reduced by increasing the beam semi-angle. While a larger beam semi-angle reduces the diffraction limited spot size, at the same time the chromatic and spherical spot size contributions will increase. In the design method that we use in this work, the mechanical configuration of the tetrode mirror is optimized to allow for a maximum beam semi-angle, that is still mainly diffraction limited.

3. Numerical methods

Traditionally, aberration coefficients are calculated using aberration integrals, in the case of mirrors using time dependent perturbation algorithms instead of position dependent algorithms [22,23]. We shall rely here on the precision of modern ray trace simulations, as is also done for instance for the design of modern low-energy and photo-emission (LEEM/PEEM) microscopes [24], and additionally motivated by the given, that only axial aberrations and small beam semi-angles are considered. We performed electron ray trace simulations using the EOD software package [25–28] and extract aberration coefficients from the obtained radial coordinates of the ray trajectories at the image plane after reflection. The analyzed systems contains spatial degrees of freedom in terms of the radius of the electrode apertures [Fig. 2(b)], as well as electrical degrees of freedom in terms of the mirror, cap, and collimator lens potential. In a miniature QEM resonator setup that we are currently building, the distance between the mirror electrode and cross-over at the image plane of the system is 25 mm and the simulation results shown in the following are based on this value.

For the calculation of spherical (C_{s3} and C_{s5}) and chromatic (C_{c1}) aberration coefficients, the range of cap and lens aperture radius is varied from $R = 100 - 500$ µm. For a fixed beam energy of 2 keV, the potential of the cap electrode is varied between −800 V and −1200 V. We expect that the spacing between the cap and mirror electrode must be small compared to the radius of the cap electrode, similar to the condition for low-energy foil corrector geometries [17,18], and thus fixed the electrode spacing to $s = 100$ µm between the mirror and cap electrode. This implies that a maximum field strength of up to 12 kV/mm is considered, which is slightly above a field strength of 10 kV/mm that is normally considered feasible in an experimental electron optical setup [29,30]. The spacing between the cap, lens, and ground electrode is fixed as well at $d = 500$ µm and we only vary the radius of the various apertures as the latter offers a feasible parameter to control in (micro)fabrication and lithographic processes.

The calculation of the effect of each geometrical combination (in terms of aperture radius and cap electrode potential) is performed by first finding the lens electrode potential that allows to image the reflected beam back onto the origin. This is achieved through the following two steps:

1. A series of ray traces is performed with a marginal ray that departs from the object plane under a 4 mrad angle. At fixed mirror and cap potential, the collimator lens potential is monotonically increased until the reflected marginal ray is imaged back onto the image plane. This condition is numerically detected when two conditions are met:
   - The sign of the slope of the reflected marginal ray, at the image plane, is equal to the sign of the slope of the initial marginal ray.
   - The sign of the radial coordinate at the image plane is opposite to the former ray trace of lower collimator lens potential, indicating that the optical axis was crossed for a collimator lens potential that is higher than that of the former and smaller than that of the current calculation.
2. A full ray trace simulation is performed with the results of step 1. For determination of the third and fifth order coefficients of spherical aberration, 9 rays are traced at angles α in the range of 0 through 8 mrad. For the calculation of the chromatic aberration coefficient, the energy of the 4 mrad ray is varied in a range of ±2 V.

Because many different geometries need to be analyzed, we built a MATLAB script that manages the execution of the EOD calculations and reads the trajectory information.

3.1. Aberration coefficients and spot size calculation

The spot size of the beam at the Gaussian image plane after reflection from the mirror depends on the (aperture) semi-angle (α) of the beam. For small semi-angles, the spot size is diffraction limited, whereas at larger semi-angles the spot size is usually dictated by the chromatic and spherical aberration coefficients of the imaging system. It is common to describe spot size contributions with the Full Width (FW) of the beam that contains only a Fraction of Current (FC) of usually 50%. With this definition, the FW50 of the diffraction limited probe size is given (for an electron wave length λ) by [31],

$$d_{A50}(\alpha) = 0.54\lambda/\alpha. \tag{1}$$

The aberration coefficients are obtained from the intersect of the ray traces with the image plane. For the determination of the chromatic aberration coefficient (C_{c1}), we fit a first order linear polynomial,

$$y(\alpha) = \left(C_1 + C_{c1}\frac{\Delta E}{E}\right)\alpha. \tag{2}$$

Here, the coefficient C_1 allows for a defocus of the beam with nominal energy (E) at the image plane. The deviation of beam energy is labeled by ΔE. From the chromatic aberration coefficient, the FW50 contribution d_{C50} is obtained through [31],

$$d_{C50} = 0.6C_{C1}\frac{\Delta E_{FW50}}{E}\alpha. \tag{3}$$

From the numerically obtained ray trajectories, the third (C_{s3}) and fifth (C_{s5}) order coefficients of spherical aberration are obtained by fitting the necessarily odd polynomial,

$$y(\alpha) = C_1\alpha + C_{s3}\alpha^3 + C_{s5}\alpha^5, \tag{4}$$

to the resulting data set of beam angle (α) versus image plane intersect coordinate (y). Unless elsewise specified, we refer to both C_{s3} and C_{s5} in any mention of spherical aberration (coefficients). The coefficient C_1 corresponds to the defocus of the reflected beam at the image plane. In [Fig. 3] we show an example of fitting the polynomials to the obtained ray coordinates at the image plane.

We have assessed the accuracy of the numerical ray trace calculations by analyzing the third and fifth order spherical aberration coefficients of a diode mirror, at a comparable grid size and interpolation method that we use for the flat mirror calculations. An exact analytical result for the diode mirror configuration is given by [13]. We found a relative error of 0.5% for the third order, and −3.8% for the fifth order coefficient of spherical aberration.

As we stated before, it is common to obtain the effect of spherical aberration coefficients on the spot size in terms of a FW50 contribution. When the fifth order coefficient is set to zero, the minimum FW50 is obtained at small defocus C_1 in between the Gaussian image plane and the image plane of the marginal ray, and given by [31]

$$d_{S50} = 0.18C_{s3}\alpha^3 \text{ when } (C_{s5} = 0). \tag{5}$$

When the third order coefficient is set to zero, the minimum FW50 is also obtained at a (different) defocus, and is given by [18]

$$d_{S50} = 0.0463C_{s5}\alpha^5 \text{ when } (C_{s3} = 0). \tag{6}$$

As these results are valid at a different defocus, they cannot be added into a single FW50 contribution from spherical aberration. Instead, one has to integrate the normalized weighted current $w(\alpha)$ that is contained within an infinitesimal angle $d\alpha$, in order to find the FW50 (see Appendix for details). This calculation requires the inverse function $\alpha = \alpha(y)$ of [Eq. (4)] for which no analytical solution is available, and instead must be solved numerically (see Appendix for details in implementing this in MATLAB).

An interesting case arises when the signs of C_{s3} and C_{s5} are opposite. Then, as a function of increasing semi-angle α, the rays are first found on one side of the optical axis, and at increasing ray angle at the other side of the optical axis as well. This effect reduces the growth of the spherical spot size, and the spot size can be further reduced by setting the proper defocus of the beam through C_1.

The total spot size is determined by a root-power-sum of its components, in which the powers are not trivially 2 [32]. However, the coefficients for the root-power-sum from literature assume only the presence of a C_{s3}, and not the C_{s5} term when weighting the contribution of spherical aberration to the total spot size. Since the addition of C_{s5} shifts the optimum defocus plane as well, we can no longer rely on the conventional summing method. Instead, we fall back here to squared addition of terms, in the absence of a better alternative. The total probe size of the system is then given by

$$d_{FW50} = \sqrt{d_{S50}^2 + d_{C50}^2 + d_{A50}^2}. \tag{7}$$

In the case of a spherical aberration limited spot size, the squared addition of the spherical and diffraction limited contribution (instead of the conventional power 4), will then result in an overestimation of the spot size contribution for these two terms.

4. Design of the tetrode mirror

We have numerically obtained electron ray trajectories for a range of cap and collimator radii, while using the cap and lens potentials to obtain 1x magnification. We refer all potentials to ground potential, which is where the beam energy is 1990 V. The mirror electrode potential is fixed at −2000 V. We only make use of accelerating lens potentials as this results in a larger spread of the beam in front of the mirror electrode, in comparison to when a decelerating lens potential is used. In principle, an optimization routine could be used to find the best values for these parameters [28,33], but this approach is not pursued at this point. The axial aberration coefficients that were obtained through these calculations are used to determine the FW50 spot size (containing 50% of the current) for each system configuration for a range of semi-angles, after reflection, and for 1x magnification imaging to the image plane. From the resulting data set the system configurations that result in the minimum spot size as a function of semi-angle after reflection are obtained.

4.1. Coarse parameter sweep

The first design step consists of a coarse parameter sweep across lens and cap electrode radii, and cap potential. A total of 405 systems [for configurations, see Table 1] are analyzed during this step. This results in a large data set that relates the system configuration parameters and the resulting aberration coefficients.

From the obtained data, it is observed that for the third order spherical aberration coefficient both positive and negative values are obtained [Fig. 4(a)]. In the figure, the white line indicates the contour at which the coefficient equals zero, and negative values are found in between the two contour lines. We observe that the coefficients mainly vary as a function of the cap radius, and are less sensitive to changes in the lens electrode radius. Note that for some configurations, we could not obtain a 1x magnified reflected beam at the image plane, and these data points are indicated by the white tiles in the plot.

The data for the fifth order spherical aberration coefficient [Fig. 4(b)] is mainly positive valued in the studied parameter range, and shows a decrease as a function of increasing cap radius, with a local maximum at a cap radius of approximately 300 μm.

For the first order chromatic aberration coefficient we obtained both positive and negative contributions as well [Fig. 4(c)]. Similar to what is observed for the spherical aberration coefficients, we notice that also the chromatic coefficient is more sensitive to the value of the cap electrode radius rather than the lens electrode radius.

We are looking for the system configuration that allows us to minimize the spot size at the image plane, after reflection at the flat mirror. The spherical spot size (due to C_{s3} and C_{s5}) is minimized by

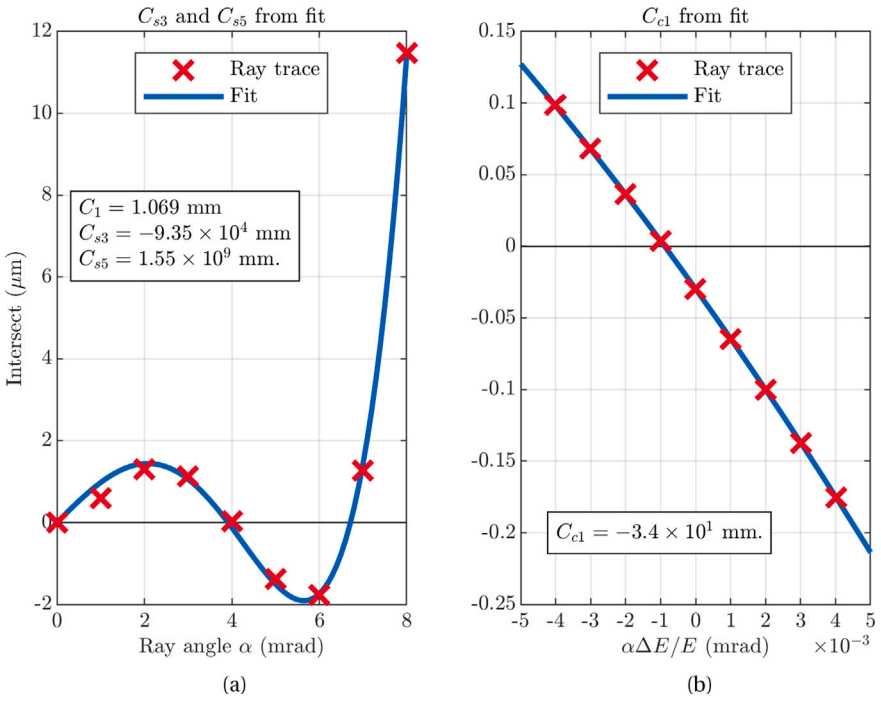

Fig. 3. Aberration coefficients are obtained by fitting a necessarily odd valued polynomial (a) for spherical aberration coefficients (C_{s3} and C_{s5}) and defocus (C_1), through the intersect of the ray trajectories at the image plane as a function of ray angle [ref. Eq. (4)], and (b) for the chromatic aberration coefficient through the product of $\alpha\Delta E/E$ [ref. Eq. (2)]. The relative error in (a) is approximately 10%, and larger than that for small ($\alpha \leq 1$ mrad) ray angles.

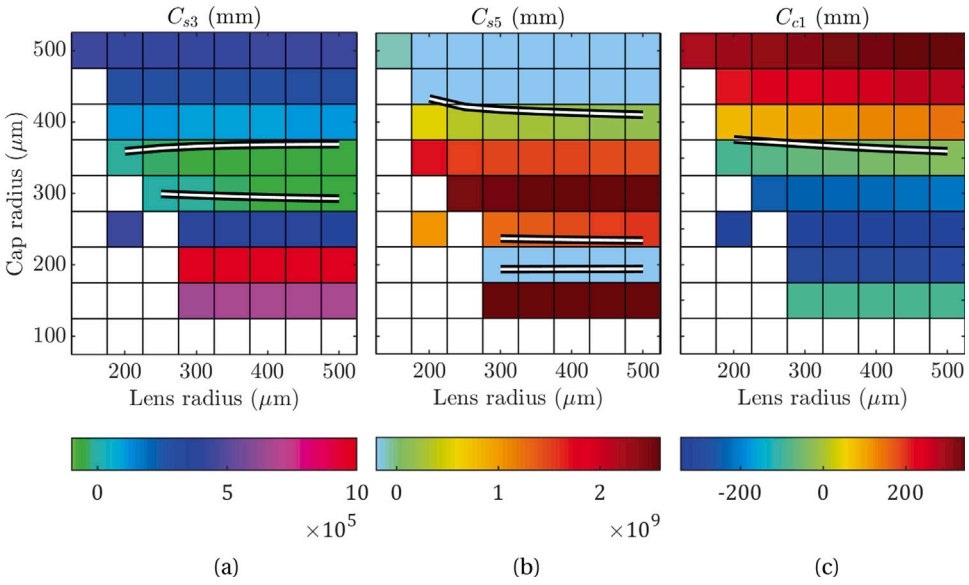

Fig. 4. Aberration coefficients as a function of the lens and cap electrode radius, at a cap potential of −1000 V. (a) Third order and (b) fifth order spherical aberration coefficient, and (c) first order chromatic aberration coefficient, obtained from the coarse parameter sweep. White lines indicate (interpolated) zero-contours in the respective data set.

selecting a region in which the two coefficients have opposite signs. This way, the one coefficient suppresses the influence of the other coefficient on the increase of spot size for a range of semi-angles (also see [Fig. 3(a)]), similarly as to how a negative defocus allows one to partially correct for the spot size degradation due to a positive C_{s3} in electron microscopes. From the shown data, it is observed that a large region satisfies the criterion of opposite signs.

4.2. Fine parameter sweep

In the second design step, the ray trace calculations are repeated in a reduced region of the parameter space and at a finer grid step size [for details, see Table 2]. The new parameter space for the cap electrode radius is based on the observation that both spherical and chromatic aberrations are near zero in the region, for which $R_{cap} \sim 300 - 400$ µm. For the lens electrode radius, no such distinct selection criteria is apparent. We selected the region, for which $R_{lens} \sim 200 - 300$ µm, based on the observation that the chromatic aberration coefficient increases at higher lens radii. The aberration coefficients that are obtained at this stage are shown in [Fig. 5]. A zero-aberration coefficient value contour line is provided for the third order spherical and the first order chromatic aberration coefficient (white lines). Only positive values for the fifth order spherical coefficient are obtained in this reduced parameter space.

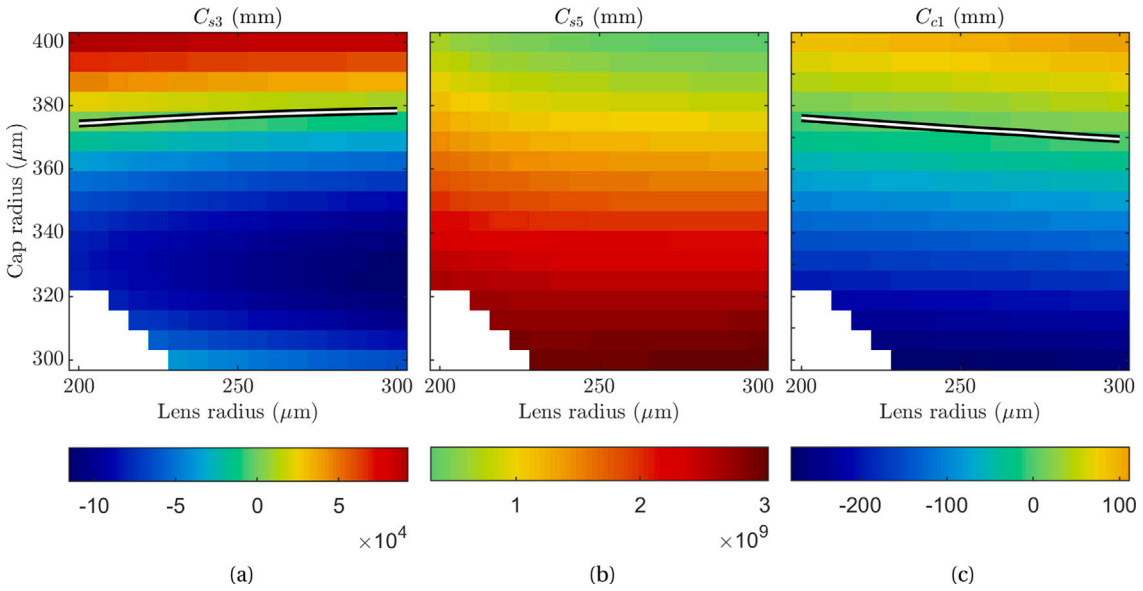

Fig. 5. Aberration coefficients as a function of the lens and cap electrode radius at −1050 V cap potential. (a) Third order and (b) fifth order spherical aberration coefficient, and (c) first order chromatic aberration coefficient, obtained from the fine parameter sweep. White lines indicate (interpolated) zero-contours in the respective data set.

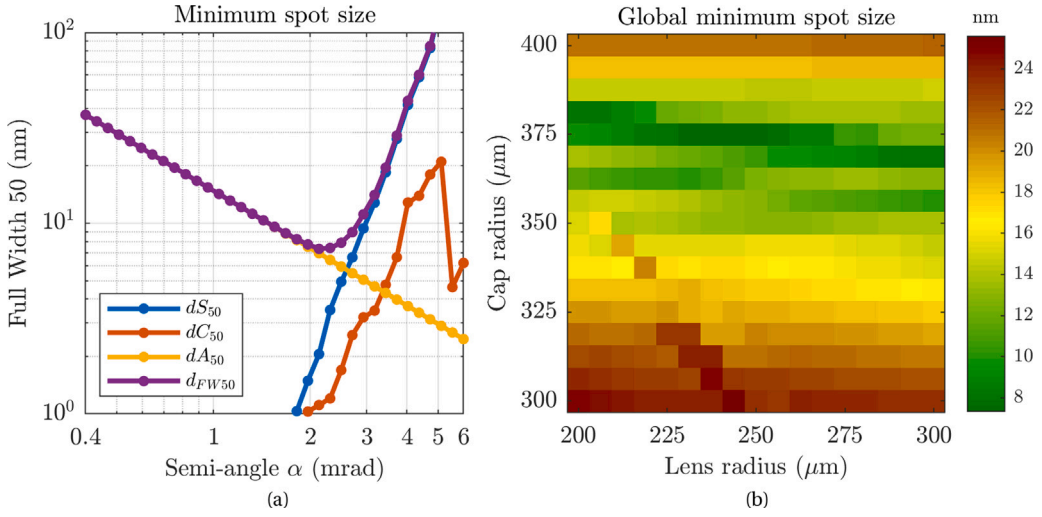

Fig. 6. (a) (Contributions to) the best resolution out of all systems, as a function of semi-angle. Indicated are the spherical (blue), chromatic (orange), diffraction (yellow), and total (purple) FW50 spot size. (b) Global minimum spot size per mechanical configuration. (For interpretation of the references to color in this figure legend, the reader is referred to the web version of this article.)

Table 1
Overview of system configurations that were analyzed in the numerical study. The actual used lens potential is interpolated from the data.

Label	Property	Range	Step	Unit
R_C	Cap radius[a]	100 ⋯ 500	50	µm
R_L	Lens radius[a]	100 ⋯ 500	50	µm
R_G	Ground radius	500	–	µm
U_M	Mirror potential	−2000	–	V
U_C	Cap potential[a]	−800 ⋯ − 1200	100	V
U_L	Lens potential	1000 ⋯ 8000	200	V
$\mathscr{E}$	Electron beam energy	−1990	–	V
s	Mirror cap spacing	100	–	µm
f	Focal length	25	–	mm
t	Electrode thickness	300	–	µm

[a]Denote independent variables, the range of other properties denote practical limitations in order to provide reasonable field strengths.

Table 2
Fine parametric sweep limits and grid step sizes.

Label	Property	Range	Step	Unit
R_C	Cap radius (*)	300 ⋯ 400	6.25	µm
R_L	Lens radius (*)	200 ⋯ 300	6.25	µm
U_C	Cap potential (*)	−900 ⋯ − 1100	50	V

The new data set provides more smooth data since the grid resolution is enhanced in comparison to the coarse parameter sweep. It is now clearly observed that a local minimum for which $C_{s3} < 0$ is formed for cap electrode radii of approximately 330 µm. Larger cap electrode radii lead to an increase in C_{s3}, and simultaneously a decrease in C_{s5}. Within the new data set, it is visible that the conditions for $C_{s3} = 0$ and $C_{c1} = 0$ coincide within a narrow band. It is thus to be expected that a minimum spot size will be obtained for $R_{cap} \sim 375$ µm, and relatively independent of the lens electrode radius.

4.3. Dependence of aberration coefficients on design parameters

The minimum spot size of the tetrode mirror system depends on the beam semi-angle. For small semi-angles, the spot size is usually diffraction limited and at larger semi-angles spherical and chromatic effects will dominate the spot size. We obtained the spot size for all system configurations that are part of the fine parameter sweep, by means outlined in Section 3.1.

The calculation is performed for various semi-angles in the range $0.4 \leq \alpha \leq 6$ mrad, at 35 equally logarithmically spaced values. For each system configuration, the spherical FW50 spot size contribution is obtained by varying the defocus C_1 [ref. Eq. (4) and Appendix for details]. The chromatic FW50 spot size contribution (d_{C50}) is obtained for a nominal beam energy of 2 keV, and a FW50 energy spread of 0.3 eV that we can achieve in experiments with a monochromatized beam emitted from a Schottky source. This results in a new data set, that contains the (contributions to the) FW50 spot size of each system, at each semi-angle.

For each semi-angle, the system configuration that provides the smallest total FW50 spot size (d_{FW50}) is obtained from this new data set. The resulting subset of data is shown in [Fig. 6(a)], and provides the minimum spot size that can be obtained as a function of beam semi-angle. From this data, we note that the spot size can be kept diffraction limited for semi-angles up to $1.5-2$ mrad. A global minimum FW50 spot size of $d_{FW50} = 7.6$ nm is found at a semi-angle of 2.3 mrad, and requires a defocus of $C_1 = 3.3$ µm. At increasing semi-angles, the minimum spot size becomes limited by the spherical aberration of the systems.

The obtained minimum spot size for each mechanical configuration in terms of lens and cap electrode radius is plotted in [Fig. 6(b)]. From this data, it is noted that the global minimum spot size is obtained for a cap electrode radius of $R_{cap} = 375$ µm, and a lens electrode radius of $R_{lens} = 250$ µm. For the electrical configuration a cap electrode potential of $U_{cap} = -1050$ V is found. In order to focus the beam with 1x magnification onto the sample plane after reflection, a lens potential of $U_{lens} = 3.5$ kV was obtained from the EOD calculations. Consequently, a maximum field strength of $E = 9.5$ kV/mm is present in the tetrode mirror, which is considered feasible in electron optical setups.

The global minimum spot size that we show in [Fig. 6(b)] seems to closely follow the zero contour line of the chromatic aberration coefficient that is plotted in [Fig. 5(c)]. This suggests that the chromatic aberration has a strong influence on the spot size of the reflected beam at the image plane, and should be chosen close to zero. After that, the effect of spherical aberration on the spot size at the image plane can be balanced by a proper amount of defocus. It should be noted that the slope of the spherical spot size contribution in [Fig. 6(a)] scales proportional with α^5. From this we can conclude that the smallest spot size at the image plane after reflecting on the flat electron mirror is limited either by diffraction, or by the fifth order aberration coefficient.

5. Discussion and conclusion

We obtained geometries for tetrode electron mirror systems with a flat surface of reflection, that exhibits only small axial aberrations. As a result, the FW50 spot size at the image after reflection from the flat mirror surface remains mainly diffraction limited for semi-angles up to $1.5-2$ mrad, at a beam energy of 2 keV. The ability to correct for axial aberrations by means of the tetrode mirror mechanical configuration, rather than additional optical components, or superimposed mirror topographies, opens new possibilities for the use of electron mirrors in general, and for repetitive imaging systems and phase plates in particular.

The low beam energy (2 keV) in our study allows for the sub-millimeter dimensions of the aperture radius. The sub-millimeter dimensions that are involved allow for lithographic fabrication processes. The use of lithographic processes allows for the fabrication of very round apertures, that show virtually no astigmatism when properly aligned to one another [21]. The alignment of individual lens electrodes can be routinely performed with our in-house built hexapod aligner [32] to within 500 nm resolution.

In conclusion, a feasible design for a topographically patternable tetrode electron mirror is described. The axial aberrations of the tetrode mirror system are minimized through careful analysis of the role of aperture dimensions of the electrodes. The successful demonstration of the proposed configuration would enable the integration of a mirror based electron beam splitter in miniature QEM setups, or reduce the number of optical components that are needed in existing electron microscopes thus offering means for increased resolving power.

Declaration of competing interest

The authors declare that they have no known competing financial interests or personal relationships that could have appeared to influence the work reported in this paper.

Acknowledgments

We acknowledge funding for this work from the Dutch Research Council (NWO), The Netherlands, and the Gordon and Betty Moore Foundation (GBMF), United States.

Appendix. Spot size as a function of defocus, in the presence of both third and fifth order spherical aberration coefficients

In this appendix we describe how to obtain the contribution to the FW50 spot size from spherical aberration in the general case, for which C_{s3}, and C_{s5} are both non-zero, and may have opposite sign. The method can be directly extended to include higher orders as well. This method is not only applicable to our case in which the beam is reflected by a mirror, but also for the calculation of the probe size in an aberration corrected SEM or STEM.

We assume a uniform current distribution in the imaging system. When the image plane coincides with the focal plane of a lens, the beam (aperture) semi-angle (α) with optical axis at the image plane, the distance between the principle optical plane of the lens and the image plane (f), and the radial distance from the optical axis at the principle optical plane of the lens system (h), are related under the small angle approximation by

$$h = \alpha f. \tag{A.1}$$

The full current (I) at the principle plane of the lens, as a function of the beam semi-angle and under the assumption of a uniform (angular) current distribution Ω is given by

$$I_{100}(\alpha) = \pi(\alpha f)^2 \Omega. \tag{A.2}$$

We can transform this into a normalized current ($\hat{I}$), which provides the current within the reduced semi-angle $[0, \tilde{\alpha}]$, which lies in the range $0 \leq \alpha \leq \tilde{\alpha}$, given by

$$\hat{I}(\tilde{\alpha}) = \left(\frac{\tilde{\alpha}}{\alpha}\right)^2. \tag{A.3}$$

Within an infinitesimal emission ring $d\alpha$ corresponding to ray angle $\tilde{\alpha}$, the contained normalized current is then given by

$$w(\tilde{\alpha}) \equiv \frac{d\hat{I}}{d\tilde{\alpha}} = \frac{2\tilde{\alpha}}{\alpha^2}. \tag{A.4}$$

Here, $w(\tilde{\alpha})$ may be regarded as a normalized weight factor, or as the fraction of current that is emitted from an infinitesimal ring.

The intersection coordinate y_S of a ray at angle $\tilde{\alpha}$ (with $0 \leq \tilde{\alpha} \leq \alpha$) at the image plane, due to defocus, and third and fifth order coefficients of spherical aberration is given by

$$y_S(\tilde{\alpha}) = \left| C_1\tilde{\alpha} + C_{s3}\tilde{\alpha}^3 + C_{s5}\tilde{\alpha}^5 \right|. \tag{A.5}$$

When the product $C_{s3}C_{s5} > 0$, i.e., the aberration coefficients are of equal sign, and with C_1 equal to zero or having the same sign, then the spherical spot size diameter FW50, containing 50% of the current, is found by solving for α_1 in

$$\int_0^{\alpha_1} w(\tilde{\alpha})d\tilde{\alpha} = 0.5 \Rightarrow FW50 = 2y_S(\alpha_1). \tag{A.6}$$

The upper limit of integration α_1 is related to y_S by inverting the latter for $\tilde{\alpha} = y_S(\tilde{\alpha})^{-1}$, and increasing $\tilde{\alpha}$ until the equality in [Eq. (A.6)] is satisfied. Inserting the obtained α_1 back into [Eq. (A.5)] then directly yields the FW50, also see [Fig. A.7(a)].

When either C_1, C_{s3}, or C_{s5} is of opposite sign of the other coefficients, and for sufficiently large coefficients, or at sufficiently large semi-angle α, the situation arises at which for increasing ray angle $\tilde{\alpha}$ the ray first crosses the optical axis at one side of the image plane, and for increasing ray angle at the other side of the image plane. Thus, for a given C_{s3} and C_{s5} of opposite sign, and C_{s5} usually but not necessarily positive, a sufficiently large semi-angle will result in a region of $\tilde{\alpha}$ for which the spot size will not increase radially outward. This situation is depicted in [Fig. A.7(b)]. A proper calculation of the spherical spot size would then require to take into account that the current that is incident from the higher ray angles $\tilde{\alpha}$ contribute a large amount of the total current, at a limited increase of spot size. To take this effect into account in the calculation of the FW50 spot size, an extension of [Eq. (A.6)] is required that allows for the additional zero-crossings of $y_S(\tilde{\alpha})$ [Eq. (A.5)] at the image plane. As we consider spherical aberration up to fifth order, in principle we expect up to five solutions [Fig. A.7(c)] to the inverse problem $\alpha = \alpha(y)$, meaning that the FW50 ($FC = 0.5$) is found by solving the following equality for α_n, with $n = 1 \cdots 5$, and for which $y_S(\alpha_1) = \cdots = y_S(\alpha_5)$,

$$\int_0^{\alpha_1} w(\tilde{\alpha})d\tilde{\alpha} + \int_{\alpha_2}^{\alpha_3} w(\tilde{\alpha})d\tilde{\alpha} + \int_{\alpha_4}^{\alpha_5} w(\tilde{\alpha})d\tilde{\alpha} = FC. \tag{A.7}$$

In order to satisfy this equality for all α_n, the inverse to [Eq. (A.5)] must be obtained, which contains 5 roots and for which to our knowledge no (practical) analytical solution exists. In the following we outline a numerical solution method that allows one to find the $FW(FC)$.

A.1. Numerical methods

The problem at hand is two-fold. On the one hand, we require up to five values for ray angles $\tilde{\alpha}$ that yield equal intersect coordinates when inserted into [Eq. (A.5)]. On the other hand, we must solve the integral in [Eq. (A.7)] using these same ray angles as integration boundaries, while satisfying the equality for the given Fraction of Current (FC). As the result of the latter calculation depends on the former, it is difficult to directly obtain the integral boundaries that exactly correspond to the FW50 case. Therefore, we suggest the following solution strategy:

1. Obtain the FW100 of the beam, for chosen beam semi-angle α.
2. Obtain the FW for a number of FW values $0 < FW \leq FW100$.
   - For a given FW, obtain the integration boundaries through the inverse of [Eq. (A.5)].
   - Perform the integral in [Eq. (A.7)], to obtain the FC related to the FW value.
3. Interpolate the obtained data set of FW and FC, in order to obtain the FW50.

A.1.1. Obtaining the FW100

The FW100 must be obtained first. This is readily performed when all coefficients are of equal sign. In that case, the FW100 is always determined by the value of the beam semi-angle, such that $FW100 = 2\times y_S(\alpha)$. In the more general case, in which the signs of the coefficients may be oppositely valued, the FW100 may be found at a smaller ray angle, as can be understood from [Fig. A.7(b)]. From the expression of local disc radius, $y_S(\tilde{\alpha}) = C_1\tilde{\alpha} + C_{s3}\tilde{\alpha}^3 + C_{s5}\tilde{\alpha}^5$, one can find the local maxima through differentiation,

$$\frac{dy_S}{d\tilde{\alpha}} = C_1 + 3C_{s3}\tilde{\alpha}^2 + 5C_{s5}\tilde{\alpha}^4 = 0. \tag{A.8}$$

Substitution of $\beta \equiv \tilde{\alpha}^2$ enables an analytical solution through the abc-formula:

$$\beta = \frac{-3C_{s3} \pm \sqrt{9C_{s3}^2 - 20C_1C_{s5}}}{10C_{s5}}. \tag{A.9}$$

From this, we obtain $\tilde{\alpha} = \sqrt{\beta}$, and only keep the real valued solutions, that satisfy $0 < \tilde{\alpha} \leq \alpha$. The FW100 is then determined by whichever term is bigger, from the set $\{y_S(\tilde{\alpha})\}$ (case in [Fig. A.7(b)]) or from the marginal ray $y_S(\alpha)$ (case in [Fig. A.7(c)]).

Note for the special case where $C_{s5} = 0$, the solution provided by [Eq. (A.9)] becomes invalid, and instead $\beta = -C_1/(3C_{s3})$ must be used.

A.1.2. Obtaining the fraction of current (FC)

After having obtained the FW100, an array of FW values in the range $0 < FW \leq FW100$ is created. We next step through these values, and obtain the (set of) ray angles α_n that correspond to the FW. This is performed in MATLAB through the use of the symbolic equation solver, as outlined in Listing 1.

Listing 1: Numerical inversion solution

```
% One-time solution for inverse a = a(y)
    problem
syms y c1 c3 c5 a;
a_inv_y = solve(y == abs(c1*a + c3*a^3 +
    c5*a^5), a);

% Update parameters based on s, to the
    inverse problem a = a(y).
copy_a_inv_y = subs(a_inv_y, [c1 c3 c5 y
    ], [s.Cs1 s.Cs3 s.Cs5 yFC]);

% copy_a_inv_y now contains the
    solutions to a, in symbolic roots.
```

In terms of execution speed, the bottleneck in this process is in finding the solution to the inverse problem numerically, and by creating the necessary symbolic variables in MATLAB for each execution of the subroutine. We noticed that the process can be sped up significantly through two distinctive methods:

1. Explicit passing along of symbolic variables and the symbolic solution of the inverse problem as an input argument to the subroutine.
2. Parallel execution (using MATLABs `parfor` method) in a high-core count system, of the for-loop in which the system configurations are looped over.

With the obtained solution $(\alpha_1, \ldots, \alpha_5)$ of the inversion problem, the Fraction of Current (FC) is obtained from the integral of [Eq. (A.7)], repeated here:

$$FC = \int_0^{\alpha_1} w(\tilde{\alpha})d\tilde{\alpha} + \int_{\alpha_2}^{\alpha_3} w(\tilde{\alpha})d\tilde{\alpha} + \int_{\alpha_4}^{\alpha_5} w(\tilde{\alpha})d\tilde{\alpha}. \tag{A.10}$$

This returns the fraction of current (FC) as a function of increasing FW. The FW50 ($FC = 0.5$) is then found through interpolation of the obtained data set of FW and FC values.

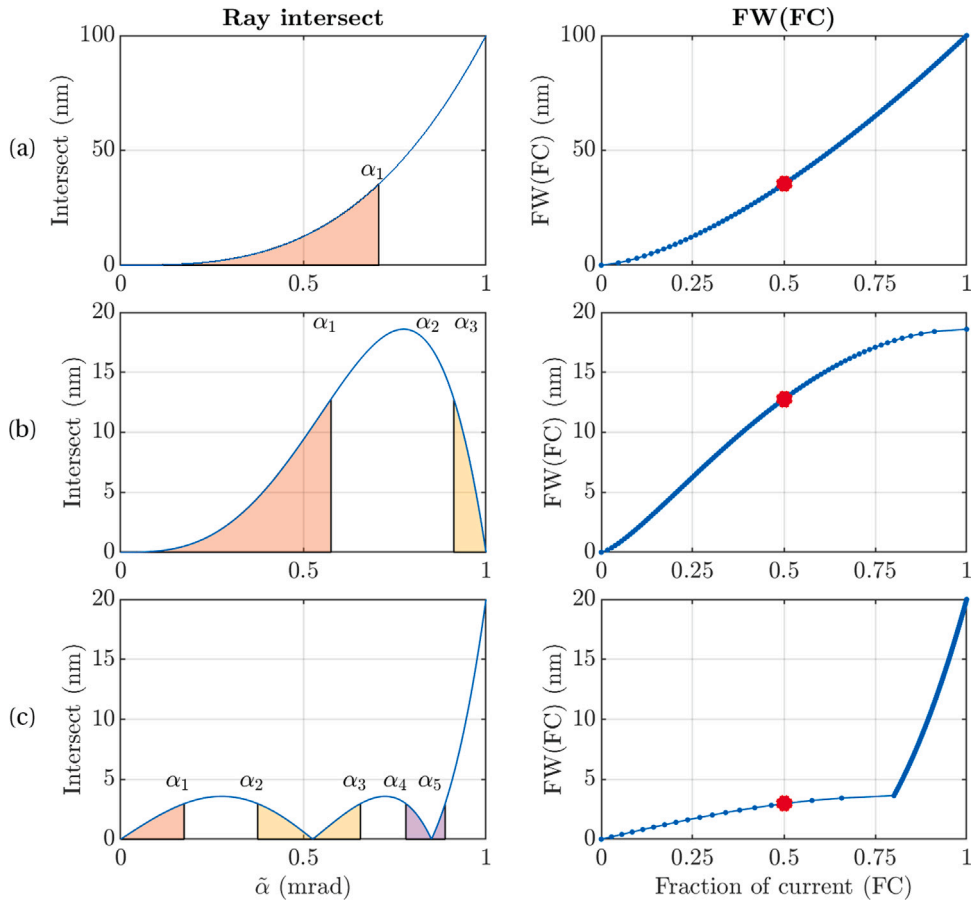

Fig. A.7. Ray trajectory intersect at the image plane as a function of ray angle. The integration domain(s) (left panels) related to the Full Width (FW) containing a Fraction of Current (FC) (right panels) is shown for three distinct cases. (a) Third order spherical aberration. (b) Third and fifth order coefficient of spherical aberration with opposite sign. (c) Negative defocus and fifth order spherical aberration coefficient, positive third order coefficient of spherical aberration.

A.1.3. Defocus leading to minimum FW50

In a practical calculation, we assume the values for C_{s3} and C_{s5} to be given and fixed. However, the defocus value C_1 could be easily changed in an experimental setup, by adjusting the lens potential. In order to obtain the minimum spherical contribution to the spot size at the image plane, the above outlined routines for finding the FW50 must be repeated at many different defocus values C_1.

To this end, we use a number of values as initial guess for the optimum defocus. For each of these defocus values, we obtain the FW50. If it happens that the smallest FW50 is obtained at the first or last defocus element in the array of guesses, the domain of initial guess values is extended into the direction of this element. This process is repeated until a local minimum FW50 is obtained, after which a refinement of the domain around the local minimum is used to further improve the calculation result.

A.2. Applications

We will now demonstrate the application of the numerical method by means of two examples.

A.2.1. Minimize C_{s3} effects through defocus of C_1

Example 1. In this example, we assume for now $C_{s5} = 0$, and a positive value for C_{s3}, say $C_{s3} = 1$ m, and a beam semi-angle of $\alpha = 1$ mrad. Initially, the system is not defocused, i.e., $C_1 = 0$. Then, the FW100 at the image plane is given by definition by $FW100 = 2 \times y_S(\alpha) = 2$ nm. This could however be reduced to $0.5C_{s3}\alpha^3 = 0.5$ nm by defocusing the beam. This is demonstrated by the blue curve in [Fig. A.8].

The minimum FW50 is much smaller, and is given by theory [31] as $0.18C_{s3}\alpha^3$, and also requires a defocus of C_1. We obtained the FW50 as a function of defocus as well (orange curve in [Fig. A.8]). The global minimum is in agreement with the theoretical expectation. From this, it is confirmed that the spot size blurring due to C_{s3} can be compensated for in part by chosen a negative C_1.

A.2.2. Minimize C_{s5} and C_{s3} effects through defocus of C_1

Example 2. The results from Example 1 might also be obtained analytically, and serve as a validation of the method. Analytical difficulties arise as soon as the third- and fifth order coefficient have opposite sign. Then, the integral boundaries in [Eq. (A.7)] can no longer be obtained analytically, and one may be led to the false conclusion that there exists a semi-angle for which the spherical spot size vanishes completely. In the following example we obtain the FW100 and FW50 at zero defocus, and compare these results to the FW50 that may be obtained by obtaining the optimum defocus value, as a function of the beam semi-angle α.

For this, we (arbitrarily) choose $C_{s3} = -1 \times 10^2$ m, and $C_{s5} = 1 \times 10^8$ m. These parameters yield the special case for which $y_S(\alpha) = 0$ at $\alpha = 1$ mrad (at zero defocus), while the Full Width containing (a Fraction of) the total Current should not vanish at this point, as for ray angles $\tilde{\alpha} < \alpha$, the ray crosses the image plane of-axis.

With the above parameters, the FW100, and FW50 (at zero and best defocus) are obtained numerically. The results of the calculation are shown in [Fig. A.9]. The blue dotted line indicates the value of $2 \times y_S(\alpha)$, i.e. full width of the transverse coordinate of the marginal

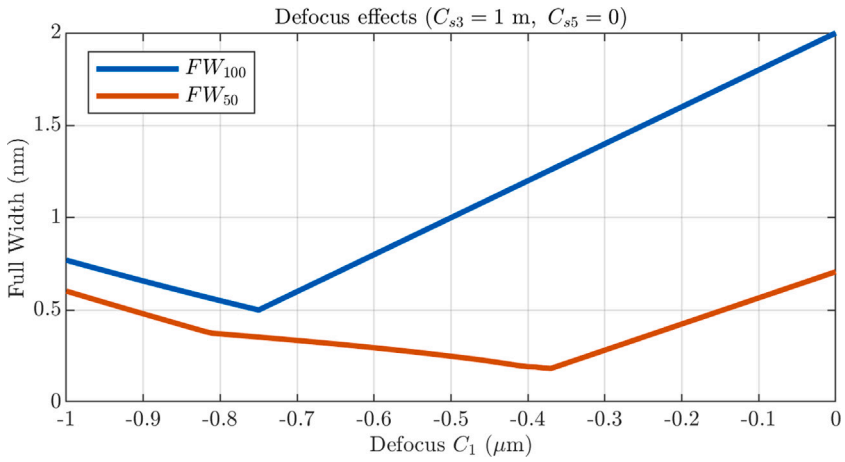

Fig. A.8. FW50 as a function of C_1 defocus, at a semi-angle of 1 mrad and C_{s3} of 1 m. At zero defocus, the obtained FW50 equals 0.5 nm. The global minimum is found at 370 nm defocus, and provides a FW50 of 0.18 nm. Both values are in agreement with the theory. (For interpretation of the references to color in this figure legend, the reader is referred to the web version of this article.)

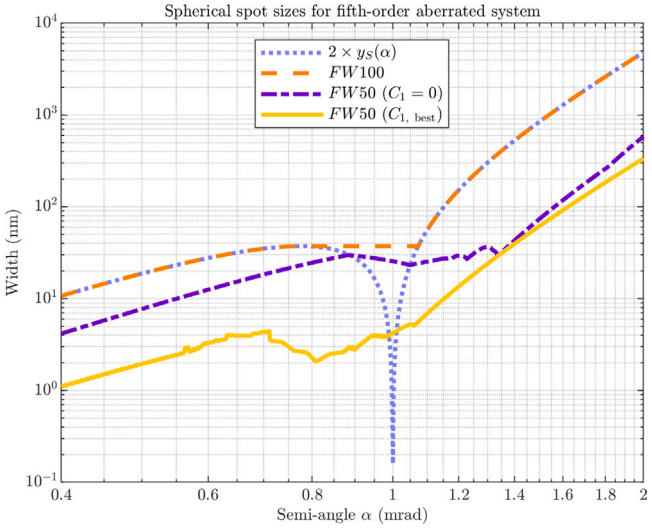

Fig. A.9. FW100 and FW50 (with and without optimizing the defocus C_1). Function $2 \times y_{100}(\alpha)$ indicates the full width of a single ray at the given semi-angle value, and is plotted for reference. (For interpretation of the references to color in this figure legend, the reader is referred to the web version of this article.)

(outermost) ray at the image plane, at zero defocus. The orange dashed curve represents the FW100, and should satisfy that it equals the global maximum $\max(2 \times y_S(\alpha))$ in the range $[0, \alpha]$. This behavior is indeed observed in the plot.

More of interest is the behavior of the FW50 spot size diameter (purple double dashed line), that indicates the diameter of the beam containing 50% of the current at zero defocus. At increasing semi-angle, it is observed that the FW50 first increases monotonically. However, around $\alpha = 0.9$ mrad a local maximum is observed. This is explained by the decrease of y_S around this semi-angle, which means that a large amount of the total current is hardly contributing to the probe size at this point (also see [Fig. A.7(b)]). This effect extends for semi-angles of up to approximately 1.35 mrad, after which the fifth order aberration becomes dominant and the spot size increases rapidly again.

Finally, the yellow curve indicates the FW50 that could be achieved when properly defocusing the system through C_1. The result indicates a large reduction in spot size diameter compared to the non-defocused case.

References

[1] A.B. Bok, J.B. le Poole, J. Roos, H. de Lang, Mirror electron microscopy, in: Advances in Imaging and Electron Physics, Elsevier, 2017, pp. 99–192.

[2] S.A. Nepijko, N.N. Sedov, Aspects of mirror electron microscopy, in: Advances in Imaging and Electron Physics, Elsevier, 1997, pp. 273–323.

[3] S.M. Kennedy, C.X. Zheng, W.X. Tang, D.M. Paganin, D.E. Jesson, Caustic imaging of gallium droplets using mirror electron microscopy, Ultramicroscopy 111 (5) (2011) 356–363.

[4] C.X. Zheng, W.X. Tang, D.E. Jesson, Asymmetric coalescence of reactively wetting droplets, Appl. Phys. Lett. 100 (7) (2012) 071903.

[5] J.C. Dupuy, A. Sibai, B. Vilotitch, Mirror Electron Microscopy (MEM): Work function and imaging of an electron beam biased junction of silicon (100), Surf. Sci. 147 (1) (1984) 191–202.

[6] M.A.R. Krielaart, P. Kruit, Grating mirror for diffraction of electrons, Phys. Rev. A 98 (6) (2018).

[7] M. Turchetti, C.S. Kim, R. Hobbs, Y. Yang, P. Kruit, K.K. Berggren, Design and simulation of a linear electron cavity for quantum electron microscopy, Ultramicroscopy 199 (2019) 50–61.

[8] P. Kwiat, H. Weinfurter, T. Herzog, A. Zeilinger, M.A. Kasevich, Interaction-free measurement, Phys. Rev. Lett. 74 (24) (1995) 4763–4766.

[9] P. Kruit, R.G. Hobbs, C.S. Kim, Y. Yang, V.R. Manfrinato, J. Hammer, S. Thomas, P. Weber, B. Klopfer, C. Kohstall, T. Juffmann, M.A. Kasevich, P. Hommelhoff, K.K. Berggren, Designs for a quantum electron microscope, Ultramicroscopy 164 (2016) 31–45.

[10] M.A.R. Krielaart, D.J. Maas, S.V. Loginov, P. Kruit, Miniature electron beam separator based on three stacked dipoles, J. Appl. Phys. 127 (23) (2020) 234904.

[11] E.G. Ramberg, Aberration correction with electron mirrors, J. Appl. Phys. 20 (2) (1949) 183–186.

[12] G.F. Rempfer, A theoretical study of the hyperbolic electron mirror as a correcting element for spherical and chromatic aberration in electron optics, J. Appl. Phys. 67 (10) (1990) 6027–6040.

[13] D. Preikszas, H. Rose, Correction properties of electron mirrors, J. Electron Microsc. 46 (1) (1997) 1–9.

[14] Z. Shao, X.D. Wu, Properties of a four-electrode adjustable electron mirror as an aberration corrector, Rev. Sci. Instrum. 61 (4) (1990) 1230–1235.

[15] P.W. Hawkes, Examples of electrostatic electron optics: The farrand and elektros microscopes and electron mirrors, Ultramicroscopy 119 (2012) 9–17.

[16] S.A. Koppell, M. Mankos, A.J. Bowman, Y. Israel, T. Juffmann, B.B. Klopfer, M.A. Kasevich, Design for a 10 keV multi-pass transmission electron microscope, Ultramicroscopy 207 (2019) 112834.

[17] R.H. van Aken, C.W. Hagen, J.E. Barth, P. Kruit, Low-energy foil aberration corrector, Ultramicroscopy 93 (3–4) (2002) 321–330.

[18] R.H. van Aken, D.J. Maas, C.W. Hagen, J.E. Barth, P. Kruit, Design of an aberration corrected low-voltage SEM, Ultramicroscopy 110 (11) (2010) 1411–1419.

[19] Z. Shao, X.D. Wu, Adjustable four-electrode electron mirror as an aberration corrector, Appl. Phys. Lett. 55 (26) (1989) 2696–2697.

[20] R.T. Hamarat, J. Witzani, E.M. Hörl, Electron optical characteristics of a concave electrostatic electron mirror for a scanning electron microscope, Scanning 6 (1) (1984) 75–79.

[21] P. Kruit, The role of MEMS in maskless lithography, Microelectron. Eng. 84 (5–8) (2007) 1027–1032.

[22] H. Rose, D. Preikszas, Time-dependent perturbation formalism for calculating the aberrations of systems with large ray gradients, Nucl. Instrum. Methods Phys. Res. A 363 (1–2) (1995) 301–315.
[23] H. Dohi, P. Kruit, Design for an aberration corrected scanning electron microscope using miniature electron mirrors, Ultramicroscopy 189 (2018) 1–23.
[24] R.M. Tromp, J.B. Hannon, A.W. Ellis, W. Wan, A. Berghaus, O. Schaff, A new aberration-corrected, energy-filtered LEEM/PEEM instrument. I. Principles and design, Ultramicroscopy 110 (7) (2010) 852–861.
[25] B. Lencová, J. Zlámal, A new program for the design of electron microscopes, Physics Procedia 1 (1) (2008) 315–324.
[26] J. Zlámal, B. Lencová, Development of the program EOD for design in electron and ion microscopy, Nucl. Instrum. Methods Phys. Res. A 645 (1) (2011) 278–282.
[27] J.E. Barth, B. Lencová, G. Wisselink, Field evaluation from potentials calculated by the finite element method for ray tracing: the slice method, Nucl. Instrum. Methods Phys. Res. A 298 (1–3) (1990) 263–268.
[28] H.W.G. van der Steen, J.E. Barth, J.P. Adriaanse, Engineering constraints and computer-aided optimization of electrostatic lens systems, Nucl. Instrum. Methods Phys. Res. A 298 (1–3) (1990) 377–382.
[29] H. Okamoto, Adaptive quantum measurement for low-dose electron microscopy, Phys. Rev. A 81 (4) (2010).
[30] A.M. Carroll, Pattern generators for reflective electron-beam lithography (REBL), in: Advances in Imaging and Electron Physics, Elsevier, 2015, pp. 1–23.
[31] P. Kruit, Electron sources, in: C.B. Carter, D.B. Williams (Eds.), Transmission Electron Microscopy, Springer International Publishing, 2016, pp. 1–15.
[32] A.C. Zonnevylle, Individual Beam Control in Multi Electron Beam Systems (Ph.D. thesis), Delft University of Technology, 2017, Ch. 5.
[33] N.H.M. Nezhad, M.G. Niasar, C.W. Hagen, P. Kruit, Local versus global optimization of electron lens system design, in: 2020 IEEE 6th International Conference on Optimization and Applications (ICOA), IEEE, 2020.